THE JOURNAL OF PHYSICAL CHEMISTRY C

Article

Cite This: J. Phys. Chem. C 2018, 122, 7088−7093

pubs.acs.org/JPCC

# Plasmonic Silver Nanoparticle-Impregnated Nanocomposite $BiVO_4$ Photoanode for Plasmon-Enhanced Photocatalytic Water Splitting

Sang Yun Jeong,[†,∥] Hye-Min Shin,[†,∥] Yong-Ryun Jo,[†] Yeong Jae Kim,[‡] Seungkyu Kim,[†] Won-June Lee,[†] Gil Ju Lee,[‡] Jaesun Song,[†] Byung Joon Moon,[§] Sehun Seo,[†] Hyunji An,[†] Sang Hyun Lee,[§] Young Min Song,[‡] Bong-Joong Kim,[†] Myung-Han Yoon,[*,†] and Sanghan Lee[*,†]

[†]School of Materials Science and Engineering and [‡]School of Electrical Engineering and Computer Science, Gwangju Institute of Science and Technology, 123 Cheomdangwagi-ro, Buk-gu, Gwangju 61005, Republic of Korea

[§]Institute of Advanced Composite Materials, Korea Institute of Science and Technology, 92 Chudongro, Bongdong-eup, Wanju-gun, Joellabuk-do 55324, Republic of Korea

Supporting Information

**ABSTRACT:** Herein, we developed a fully solution-deposited nanocomposite photoanode based on silver nanoparticle (NP)-impregnated bismuth vanadate ($BiVO_4$) films. The synthesized Ag NPs exhibit diameters of few nanometers and uniform matrix dispersion, which were confirmed by high-resolution transmission electron microscopy. The photoanode composed of the Ag NP-incorporated nanocomposite $BiVO_4$ showed a remarkable enhancement in both low potential and the saturated photocatalytic current densities in comparison with the pristine $BiVO_4$ film. The observed experimental results are attributed to the improved carrier generation and enhanced charge separation by the localized surface plasmon resonance-mediated effect as suggested by electrochemical impedance spectroscopy and a numerical simulation.

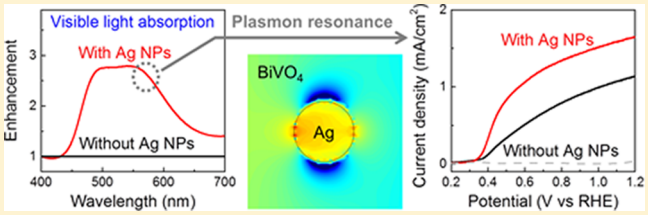


## INTRODUCTION

Recently, the energy-harvesting technology based on photocatalytic water splitting has drawn significant attention because it utilizes the unlimited free energy resources such as solar energy. In the early stage of the photocatalysis research, titanium dioxide ($TiO_2$) has been intensively investigated as a photoanode because of its natural abundance and stability during the reaction.[1−3] However, the photocatalytic performances of $TiO_2$-based photocatalysts are poor because $TiO_2$ has a large band gap of 3.2 eV (388 nm); thus, the light absorption is limited to the near-UV region (<400 nm). To overcome this issue, harnessing the localized surface plasmon resonance (LSPR) in metal nanoparticles (NPs) has been proposed as one of the possible solutions. The LSPR represents the response of oscillatory electrons in metal with respect to the incident light wave. Because a peak resonant wavelength of the given metal NP can be tailored to the visible region by controlling its size and shape,[4,5] the NP-modified $TiO_2$ photocatalysts exhibit photocatalytic activity under the illumination of visible light.[6−8] This strategy is particularly referred to as "plasmonic photocatalysis" and has been applied to the other oxides such as bismuth vanadate ($BiVO_4$),[9−14] hematite ($\alpha$-$Fe_2O_3$),[15] and tungsten oxide ($WO_3$).[12] Among them, $BiVO_4$ is one of the most intensively studied materials because the monoclinic $BiVO_4$ shows a small band gap (~2.4 eV) and favorable band edge position with respect to the water redox potential.[11,17−29]

Solution-based techniques for fabricating various photocatalysts including the plasmonic photocatalysis materials have been employed by many research studies because of their low cost and facile composition variation. However, most of the previous studies regarding the solution-deposited NP-based photocatalyst development show that metal NPs were partially embedded into or tethered on the surface of the semiconductor layer.[11,18−26] In the cases of both structures, the full utilization of LSPR-induced enhancement effects is limited because the penetration depth of the LSPR-induced electric field is very short; thus, the carrier generation occurs only in the finite region of semiconductor in the vicinity of metal NPs (a few nanometers from the metal surface).[4]

Herein, we developed the fully solution-deposited silver (Ag) NP-impregnated nanocomposite $BiVO_4$ (Ag−$BiVO_4$) photoanode for maximum utilization of LSPR-induced enhancement effects. The Ag NP was chosen because its resonant wavelength (360−500 nm) well matches with the absorption edge of $BiVO_4$ (~520 nm).[4] The proposed synthesis method is exceptionally simple based on all solution-based techniques, as described in Figure 1. We fully examined the structural characteristics and photocatalytic performance of the synthesized Ag−$BiVO_4$ film while the Ag concentration was varied and compared these results with those from the pristine $BiVO_4$. Furthermore, the observed contribution of the LSPR-induced enhancement at various Ag NP contents was investigated

Received: January 8, 2018
Revised: March 10, 2018
Published: March 11, 2018






DOI: 10.1021/acs.jpcc.8b00220
J. Phys. Chem. C 2018, 122, 7088−7093

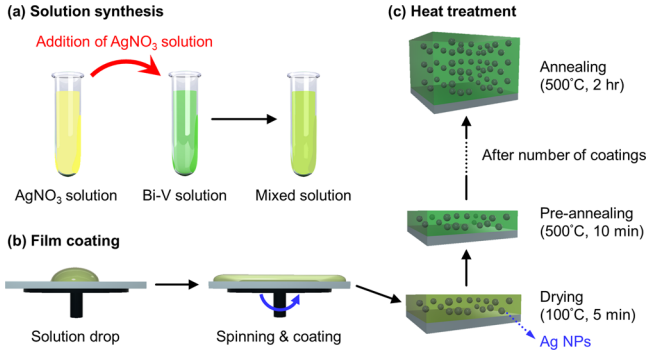


**Figure 1.** Schematic illustrations of the synthesis procedures of the Ag NP-impregnated nanocomposite $BiVO_4$ film. Details of each procedure are described in Experimental Section.

comprehensively by analyzing the observed photocatalysis characterizations in conjunction with the results obtained from photoluminescence (PL) spectroscopy and numerical simulations.

## EXPERIMENTAL SECTION

**Materials for Synthesizing Ag−$BiVO_4$.** Bismuth(III) nitrate pentahydrate ($Bi(NO_3)_3{\cdot}5H_2O$, 98%, Alfa Aesar), vanadyl acetylacetonate ($VO(acac)_2$, 98%, Alfa Aesar), acetylacetone (99.5%, Fluka), silver nitrate ($AgNO_3$, 99.9%, Alfa Aesar), *N*,*N*-dimethylformamide (99.8%, Aldrich), sodium sulfate ($Na_2SO_4$, 99%, Aldrich), and sodium sulfite ($Na_2SO_3$, 99%, Aldrich) were purchased and utilized without further purification.

**Fabrication of a Ag−$BiVO_4$ Film.** For the preparation of precursor solutions, we referred to the previous work reported by Pastoriza-Santos and Liz-Marzán, which shows that the reduction of silver nitrate in *N*,*N*-dimethylformamide in the presence of organosilicon compounds directly led to silica-coated silver NPs.[30] In the case of a Ag−$BiVO_4$ film, stoichiometric Bi−V solution was synthesized by dissolving 0.194 g of $Bi(NO_3)_3{\cdot}5H_2O$ and 0.106 g of $VO(acac)_2$ in 11.5 mL of acetylacetone followed by sonication. The $AgNO_3$ precursor was weighed and dissolved in 5 mL of *N*,*N*-dimethylformamide to make the $AgNO_3$ solutions with the concentrations of 20, 40, and 80 mM, followed by the addition of 0.10 mL of deionized water and sonication. Both solutions were mixed and stirred thoroughly for 10−15 min with a volume ratio of 4:1. The corresponding concentrations of $AgNO_3$ in the final solutions are 4.0, 8.0, and 16 mM. F-Doped tin oxide-coated glasses (FTO glass, Pilkington, TEC 15) were used as substrates. The size of the FTO substrates was typically 1.0 cm × 1.5 cm. Before fabrication, the FTO substrate was sonicated successively in deionized water, acetone, and isopropyl alcohol. For photocurrent measurement, the conductive FTO layer (i.e., 1.0 cm × 0.50 cm) was defined by an insulating tape. The final solution was coated on the FTO substrate by spin-coating. Then, the sample was dried at 100 °C for 5 min, followed by the thermal annealing at 500 °C for 10 min under ambient condition. Finally, after multiple coatings, the substrates were annealed at 500 °C for 2 h.

**Characterizations of Ag−$BiVO_4$ Films.** Crystalline phase analysis was performed by an X-ray diffraction (XRD) technique using Cu K$\alpha$ radiation ($\lambda$ = 1.5405 Å) with a Rigaku D/MAX-2500 X-ray diffractometer. The diffractometer was operated at 40 kV and 100 mA for the measurement of the polycrystalline $BiVO_4$ film on FTO glass. The $\theta-2\theta$ scan was measured between 10 and 55° with a scan speed of 0.1°/s. Diffuse reflectance UV−vis absorption spectra were obtained using a Varian Cary 500 Scan spectrometer. Photo-electrochemical cell (PEC) measurements were performed under an illuminated condition of 1 sun (100 mW/cm$^2$) using a 300 W Xe lamp (Newport) with an AM 1.5G filter (Newport). The photoanode substrates were sealed with the insulating epoxy except for the contact side with the electrolyte solution, the area of which was measured from the ruler-scaled photographs of each sample. The light was illuminated on the front side ($BiVO_4$) of the sample in a three-electrode glass cell through a quartz window. In our configuration, $BiVO_4$ was used as a working electrode, whereas Pt and Ag/AgCl (saturated KCl) were employed as a counter electrode and a reference electrode, respectively. The potential applied on the $BiVO_4$ electrode was measured by Ag/AgCl (saturated KCl) and calculated to the potential versus the reversible hydrogen electrode ($V_{RHE}$) through the following equation:

$$V_{RHE} = V_{Ag/AgCl} + V^0_{Ag/AgCl} + 0.059 \times pH \quad (1)$$

where $V^0_{Ag/AgCl}$ is 0.197 V at 25 °C.

Aqueous solutions of 0.5 M sodium sulfate with 0.5 M sodium sulfite were introduced as the electrolyte. Linear sweep voltammetry measurements were conducted using an Autolab PGSTAT302N potentiostat at a scan rate of 10 mV/s. Electrochemical impedance spectroscopy (EIS) and incident photon-to-current conversion efficiency (IPCE) were measured using potentiostat (nStat, Ivium Technologies). EIS was conducted with applying 1.23 V versus the reversible hydrogen electrode (RHE). PL measurement was conducted using a PL spectrophotometer (Hitachi F-7000). The structural characteristics of the Ag−$BiVO_4$ films and elemental mapping were investigated using a high-resolution transmission electron microscope (Tecnai G2 F30 S-Twin, 300 keV, FEI). The surface morphology of the sample was confirmed by field-emission scanning electron microscopy (SEM, Hitachi S-4700). Auger electron spectroscopy (AES) was carried out at an electron beam energy of 3 kV, and the measurement area was 2.0 $\mu$m × 2.0 $\mu$m for all samples (PHI 700, KIST).

**Simulation.** The electric field distribution and the optical absorption characteristics of Ag−$BiVO_4$ were calculated by the three-dimensional finite-difference time-domain (3D FDTD) method (FullWAVE, RSoft Design Group, USA) with 2000 grid points per wavelength. The simulation domain sizes in the *x*, *y*, and *z* directions were 20, 20, and 40 nm, respectively. The perfectly matched layer boundary conditions were used to isolate the computational regions. The Ag−$BiVO_4$ structures were illuminated by a normal incident plane wave with different monochromatic wavelengths (i.e., 360, 430, and 550 nm). The wave propagation monitor was located on the *x*−*z* plane ($y$ = 0) to measure the spatial absorption profile. The optical constants of Ag and water were taken from the previous literature,[31] and that of $BiVO_4$ was measured using an spectroscopic ellipsometer.

## RESULTS AND DISCUSSION

The Ag NPs in the Ag−$BiVO_4$ film were examined by transmission electron microscopy (TEM). Figure 2a−c shows the bright-field (BF) images of the Ag−$BiVO_4$ films which were synthesized using the mixed solutions with the different Ag concentrations. A lattice spacing of 0.2042 nm corresponds to


DOI: 10.1021/acs.jpcc.8b00220
J. Phys. Chem. C 2018, 122, 7088−7093

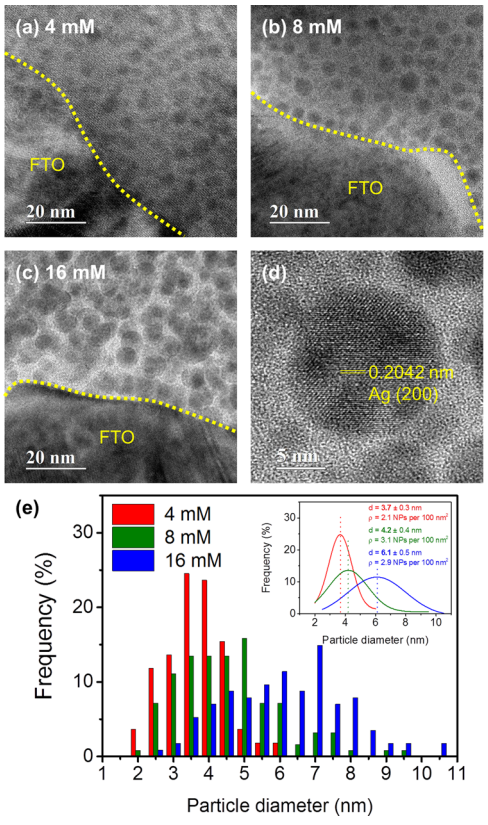


**Figure 2.** HR TEM images of the Ag–$BiVO_4$ films with different Ag concentrations of (a) 4, (b) 8, and (c) 16 mM, which show the changes in the sizes of the synthesized Ag NPs. The Ag NPs have the spherical shape and the fcc phase, as shown in (d). (e) Size distributions of the Ag NPs are measured from each HR TEM image. The mean particle diameters are 3.7 ± 0.3, 4.2 ± 0.4, and 6.1 ± 0.5 nm for the Ag concentrations of 4, 8, and 16 mM, respectively. The interface between $BiVO_4$ and FTO are represented as a dotted line in (a–c). Inset: The Gaussian plots of the data given in (e). Mean particle diameters, standard deviations, and areal densities of the Ag NPs are presented for clear comparison.

the (200) interplanar spacing of silver [face-centered cubic (fcc)], which is confirmed by the high-resolution (HR) TEM image, as shown in Figure 2d. The image also shows that the Ag which is vulnerable to oxidation is not oxidized. In addition, the elemental mapping on Ag–$BiVO_4$ confirms that the Ag NPs are dispersed in $BiVO_4$ (see Figure S1 in the Supporting Information). For an Ag concentration of 4.0 mM, it can be easily distinguished that the few-nanometer-sized spherical Ag NPs are impregnated in the $BiVO_4$ matrix (Figure 2a). However, the synthesized Ag NPs become inhomogeneous in their size and distribution for the higher Ag concentrations of 8.0 and 16 mM, as shown in Figure 2b,c, respectively. For clear comparison, the changes in the size distributions of the synthesized Ag NPs are presented in Figure 2e. The diameters (d) and the areal densities ($\rho$) of the NPs were measured from the BF TEM images of each sample. The Gaussian plots of each distribution are given in the inset of Figure 2e, in which the smallest mean diameter of 3.7 ± 0.3 nm and the narrowest size distribution are observed for a Ag concentration of 4.0 mM.

The results of the 3D FDTD simulations are given in Figures 3 and S2. The simulation results present the optimal configuration of the Ag NPs for the utilization of the LSPR effects. As shown in Figure 3, the Ag NP with the impregnated

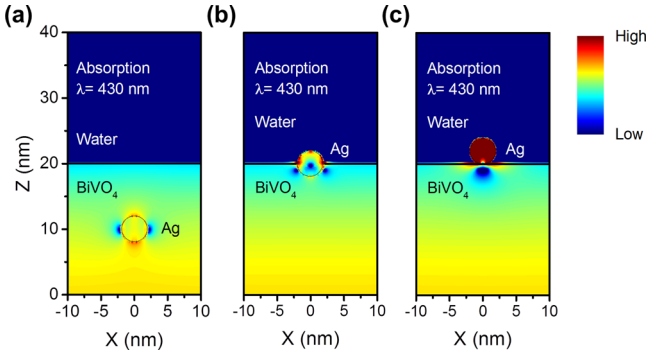


**Figure 3.** FDTD simulation results for the light absorption distribution of $BiVO_4$ and single spherical Ag NP in different configurations; (a) an impregnated, (b) a half-embedded, (c) a surface-attached configuration. The results are calculated under the irradiation of light with a wavelength of 430 nm. The size of the Ag NP is 4 nm in diameter. The electrolyte is assumed to have the same optical constants as water.

configuration (Figure 3a) reinforces the light absorption in the bulk of $BiVO_4$, whereas both the half-embedded (Figure 3b) and the surface-attached configurations (Figure 3c) affect only the near-surface region. Therefore, we confirm that the synthesized Ag–$BiVO_4$ films are in the most appropriate configuration (see Figure 3) for the maximized utilization of the LSPR-induced enhancement effects.

The physical phenomena of the plasmonic photocatalysis are at least inclusive of the following: (1) the formation of local electric field and (2) the improved light absorption originated from the oscillation of the surface plasmon in the metal NP in response to the incoming light waves and, thereby, (3) the enhanced generation of the charge carriers. These mechanisms are depicted in Figure 4. At the initial stage, the electrons in the

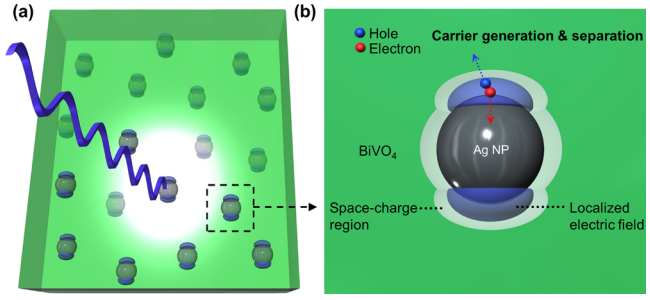


**Figure 4.** LSPR-induced enhancement mechanisms in the Ag–$BiVO_4$ films are shown in (a). The detailed mechanisms described in (b) are valid under the conditions of the formation of the electrical contact between $BiVO_4$ and impregnated Ag NPs.

Ag NPs are oscillating when transverse light waves are incoming (Figure 4a). The oscillation of electrons creates the electric field in the direction proportional to the incident light, and the intensities of the electric fields are amplified.[4] It is generally accepted that the LSPR-induced electric field at the metal surface generates active electron–hole pairs inside the semiconductor in an identical way that the electromagnetic light wave does (Figure 4b) and is considered as one of the major enhancement mechanisms. Moreover, the LSPR affects the light absorption of the surroundings. Note that these phenomena also work for Ag–$BiVO_4$, as described in Figures S2 and S3. Under the illumination of the visible light (Figure



DOI: 10.1021/acs.jpcc.8b00220
J. Phys. Chem. C 2018, 122, 7088–7093

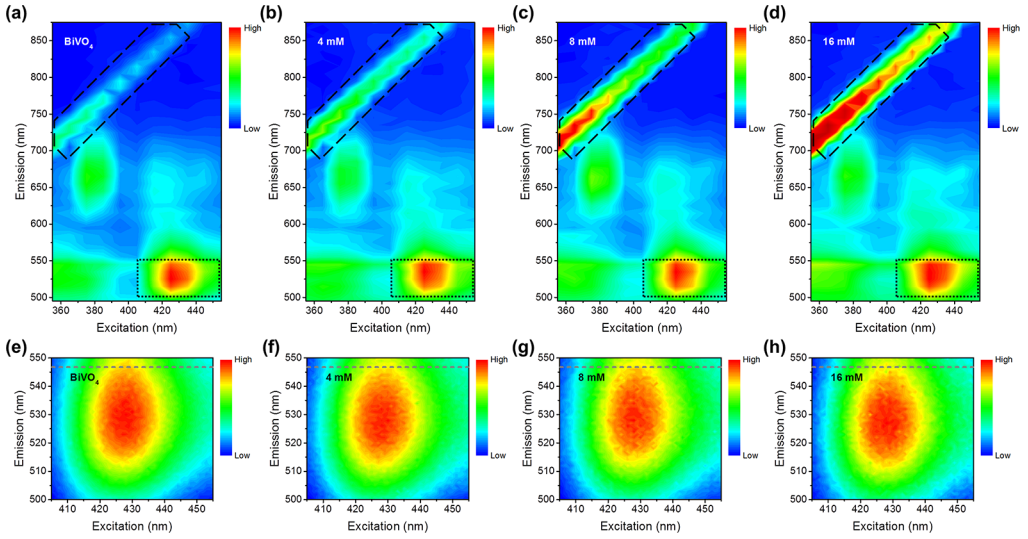


**Figure 5.** PL measurement data for the Ag−$BiVO_4$ films (a−d). Detailed mapping results (e−h) for the "dashed rectangle" in (a−d), where the PL emissions for the intraband relaxation of the electrons in $BiVO_4$ occurred. The molar concentrations given in the figure are the Ag concentrations in the precursor solution.

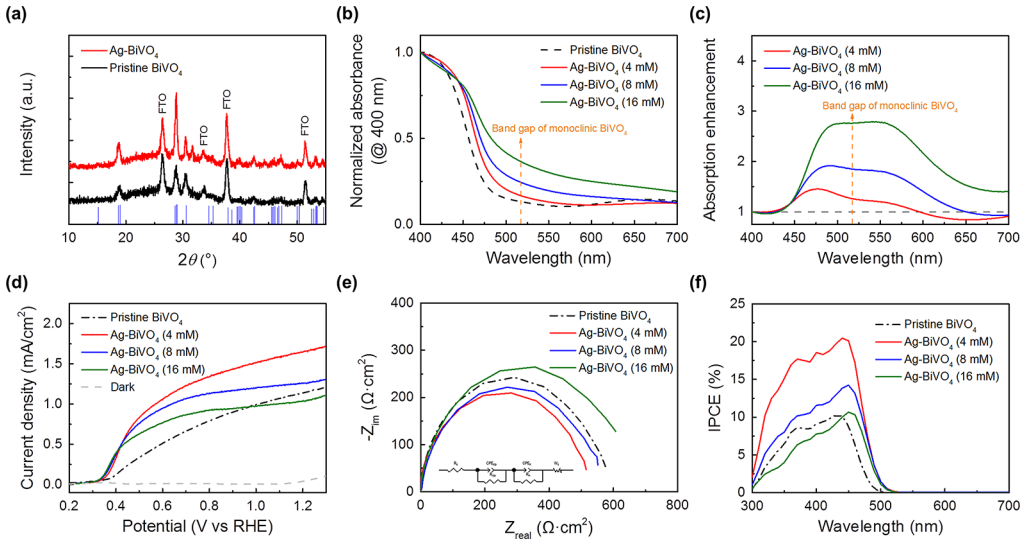


**Figure 6.** (a) XRD $\theta$−$2\theta$ scans of the pristine $BiVO_4$ and the Ag−$BiVO_4$ film with a Ag concentrations of 4 mM. The signals from the FTO glass are indicated. The vertical lines are peaks of the monoclinic $BiVO_4$ (PDF# 83-1699). (b) Normalized UV−vis absorption spectra of Ag−$BiVO_4$ and (c) absorption enhancement calculated from the data shown in (b). (d) Photo-electrochemical measurement data for the Ag−$BiVO_4$ films. The electrolyte was 0.5 M $Na_2SO_4$ aqueous solution with 0.5 M $Na_2SO_3$. (e) EIS spectra for Ag−$BiVO_4$ films. Inset: An equivalent circuit for the Ag−$BiVO_4$ films. The analysis was conducted under AM 1.5G illumination (100 mW/$cm^2$). (f) IPCE spectra of the Ag−$BiVO_4$ films conducted under simulated light illumination with applying 1.23 V vs RHE. The molar concentrations given in the figure are the Ag concentrations in the precursor solution.

S2b,e) and the UV light (Figure S2a,d), both $BiVO_4$ and Ag NP absorb the light (Figure S3) and the Ag NP generates the localized electric field by the LSPR.

The characteristics of the carrier excitation in Ag−$BiVO_4$ are investigated by the PL measurement. As shown in Figure 5a−d, the PL intensities in the "dashed area" increase with the high Ag concentrations. Because the PL intensities are proportional to the number of carrier recombination, these trends imply that the carrier concentration in Ag−$BiVO_4$ is increased as a result of the LSPR-induced effects, as described in Figure 4. In Figure 5e−h, the detailed data for the "dotted rectangle" in Figure 5a−d are given. Interestingly, the emission from the electrons generated by the band excitation in $BiVO_4$ is blue-shifted for Ag−$BiVO_4$. The origin of the shift may be attributed to the influence of the LSPR-induced electric field on the excited electrons in $BiVO_4$ or the consequence of the hot-electron injection from the Ag NPs.

The analyses for the crystalline phase and the optoelectronic behavior of the Ag−$BiVO_4$ films were performed by XRD and the UV−vis spectroscopy, respectively. The results are given in Figure 6a−c. The crystalline phase of $BiVO_4$ was analyzed. Figure 6a shows that the monoclinic $BiVO_4$ is formed in both the pristine and the nanocomposite films. Besides, in the XRD pattern of Ag−$BiVO_4$, characteristic peaks of Ag could not be distinguished, which implies that Ag exists as well-dispersed discrete NPs rather than agglomerated clusters over the entire region of the film (see Figures S4 and S5 in the Supporting Information). The UV−vis absorption spectra given in Figure



DOI: 10.1021/acs.jpcc.8b00220
J. Phys. Chem. C 2018, 122, 7088−7093

6b are normalized by the absorbance of each spectrum at 400 nm for the clear comparison, and the absorption edge of $BiVO_4$ (~517 nm) is indicated by a dotted arrow. It should be noted that the LSPR-induced visible light absorption coincides with the band gap absorption by the semiconductor. Therefore, the incorporation of the Ag NPs with $BiVO_4$ is expected to exhibit more intensive enhancement because the peak resonant wavelength of the spherical Ag NP could be tailored from 400 to 500 nm,[32,33] which is close to the absorption edge of $BiVO_4$ (~517 nm). Consequently, the enhanced light absorbance with the increased Ag concentration is observed over the visible region (Figure 6b). The absorption enhancements calculated from the data given in Figure 6b provide more distinct trends (Figure 6c). It is reported that the peak resonant wavelength strongly depends on the dielectric constant of a surrounding medium; if the medium has a higher dielectric constant, the resonant wavelength of the Ag NP is red-shifted.[4,34] Thus, considering that the peak wavelength range of 400−500 nm was obtained from the Ag NPs surrounded by air[33] or KCl[32] (a dielectric constant of 4.8[35]), the peak absorption enhancement in the red-shifted range of 450−550 nm (Figure 6c) is well-explained because our results are obtained from the Ag NPs surrounded by the $BiVO_4$ medium with a dielectric constant of 68.[36]

The photocatalytic performances of the Ag−$BiVO_4$ films were investigated by the PEC measurement. Figure 6d shows that the performances of the Ag−$BiVO_4$ films are improved in comparison with that of the pristine $BiVO_4$. In particular, the increase in the current densities in the Ag−$BiVO_4$ samples is 3.3 times higher than those of the pristine sample at 0.4 V versus the reversible hydrogen electrode (V vs RHE). In addition, the saturated current density at 1.23 V versus RHE is improved while the highest value is obtained for the optimum Ag concentration of 4.0 mM. These results can be explained in terms of the LSPR-induced enhancement mechanism. It is noteworthy that we assume that the LSPR-induced enhancement is responsible for the carrier generation and separation, not for the water redox reaction, because the Ag NPs were impregnated in the $BiVO_4$ medium. At first, the steep initial increase and the enhanced saturated current density are mainly attributed to the increased carrier concentration by the efficient charge carrier generation. Besides, the formation of the Schottky junction creates a space-charge region in the semiconductor,[5,12−16,19,37,38] and hence, the separation of the charge carriers is enhanced. Those enhancement mechanisms are observed by the EIS analysis. EIS was conducted under the illumination of light with applying 1.23 V versus RHE so that the carrier generation and separation kinetics during the oxygen evolution reaction could be evaluated. The EIS results are presented as a Nyquist plot, as shown in Figure 6e. An equivalent circuit consists of constant phase elements, resistances, and a Warburg impedance ($W_s$), as described in the inset of Figure 6e. $W_s$ is included in the circuit for better fitting results. The results are given in Table S1 (Supporting Information). Among the Ag−$BiVO_4$ films, 4 mM Ag−$BiVO_4$ has the smallest $R_{dp}$ (resistivity in the depletion region). In addition, $R_{dp}$ rises as the Ag concentration increases to 16 mM. These trends well match with the size distribution of the Ag NPs, as discussed in Figure 2; the inhomogeneity in the size and dispersion of the Ag NPs is observed for the Ag concentrations of 8.0 and 16 mM. On the other hand, the smallest diameter and the narrowest size distribution are verified for the Ag concentration of 4.0 mM. Thus, the carrier recombination in the bulk of film is less likely to happen for the latter. Consequently, the IPCE was measured to elucidate the improved efficiency by the LSPR-mediated effect. The IPCE spectra are given in Figure 6f. The results show that 4 mM Ag−$BiVO_4$ exhibits the highest efficiency with a peak at 440 nm. Clearly, the highest efficiency of 4 mM Ag−$BiVO_4$ is attributed to the maximized utilization of the LSPR-mediated effect, which is obtained by the formation of the Ag NP-impregnated configuration in the $BiVO_4$ photoanode.

## CONCLUSIONS

In summary, we aim to enhance the photocatalytic performance of $BiVO_4$ by means of the LSPR-mediated enhancement mechanisms. To achieve the goal, we have synthesized the Ag NP-impregnated $BiVO_4$ film by the fully solution-based technique. As a result, the performance of the nanocomposite film exhibited a drastic increase in the current density at low potentials and the improved kinetics of the carrier generation and separation. We believe that the synthesis method of this study is readily applicable to various photocatalytic systems containing the light-active semiconductors and the noble metal NPs such as Ag, Au, and Pt.

## ASSOCIATED CONTENT

### Supporting Information

The Supporting Information is available free of charge on the ACS Publications website at DOI: 10.1021/acs.jpcc.8b00220.

TEM elemental mapping results, additional FDTD simulation results, surface SEM images of the samples, AES spectra, and fitting results of EIS analysis (PDF)

## AUTHOR INFORMATION


### Corresponding Authors

*E-mail: mhyoon@gist.ac.kr (M.-H.Y.).
*E-mail: sanghan@gist.ac.kr (S.L.).

### ORCID

Sang Hyun Lee: 0000-0002-7784-5939
Bong-Joong Kim: 0000-0002-5335-4342
Sanghan Lee: 0000-0002-5807-864X

### Author Contributions

‖S.Y.J. and H.-M.S. contributed equally.


### Notes

The authors declare no competing financial interest.

## ACKNOWLEDGMENTS

This work was supported by the Samsung Research Funding Center of Samsung Electronics under project number SRFC-MA1402-10.

## REFERENCES


(1) Fujishima, A.; Honda, K. Electrochemical Photolysis of Water at a Semiconductor Electrode. *Nature* **1972**, *238*, 37−38.
(2) Schrauzer, G. N.; Guth, T. D. Photocatalytic Reactions. 1. Photolysis of Water and Photoreduction of Nitrogen on Titanium Dioxide. *J. Am. Chem. Soc.* **1977**, *99*, 7189−7193.
(3) Low, J.; Yu, J.; Jaroniec, M.; Wageh, S.; Al-Ghamdi, A. A. Heterojunction Photocatalysts. *Adv. Mater.* **2017**, *29*, 1601694.
(4) Zhang, X.; Chen, Y. L.; Liu, R.-S.; Tsai, D. P. Plasmonic Photocatalysis. *Rep. Prog. Phys.* **2013**, *76*, 046401.
(5) Linic, S.; Christopher, P.; Ingram, D. B. Plasmonic-Metal Nanostructures for Efficient Conversion of Solar to Chemical Energy. *Nat. Mater.* **2011**, *10*, 911−921.



DOI: 10.1021/acs.jpcc.8b00220
J. Phys. Chem. C 2018, 122, 7088−7093

(6) Awazu, K.; Fujimaki, M.; Rockstuhl, C.; Tominaga, J.; Murakami, H.; Ohki, Y.; Yoshida, N.; Watanabe, T. A Plasmonic Photocatalyst Consisting of Silver Nanoparticles Embedded in Titanium Dioxide. *J. Am. Chem. Soc.* **2008**, *130*, 1676−1680.
(7) Kumar, M. K.; Krishnamoorthy, S.; Tan, L. K.; Chiam, S. Y.; Tripathy, S.; Gao, H. Field Effects in Plasmonic Photocatalyst by Precise $SiO_2$ Thickness Control Using Atomic Layer Deposition. *ACS Catal.* **2011**, *1*, 300−308.
(8) Park, J.; Kim, H. J.; Nam, S.; Kim, H.; Choi, H.-J.; Jang, Y. J.; Lee, J. S.; Shin, J.; Lee, H.; Baik, J. M. Tow-Dimensional Metal-Dielectric Hybrid-Structured Film with Titanium Oxide for Enhanced Visible Light Absorption and Photo-Catalytic Application. *Nano Energy* **2016**, *21*, 115−122.
(9) Chen, Y.-S.; Manser, J. S.; Kamat, P. V. All Solution-Processed Lead Halide Perovskite-$BiVO_4$ Tandem Assembly for Photolytic Solar Fuels Production. *J. Am. Chem. Soc.* **2015**, *137*, 974−981.
(10) Park, Y.; McDonald, K. J.; Choi, K.-S. Progress in Bismuth Vanadate Photoanodes for Use in Solar Water Oxidation. *Chem. Soc. Rev.* **2013**, *42*, 2321−2337.
(11) Lee, M. G.; Moon, C. W.; Park, H.; Sohn, W.; Kang, S. B.; Lee, S.; Choi, K. J.; Jang, H. W. Dominance of Plasmonic Resonant Energy Transfer over Direct Electron Transfer in Substantially Enhanced Water Oxidation Activity of $BiVO_4$ by Shape-Controlled Au Nanoparticles. *Small* **2017**, *13*, 1701644.
(12) Li, J.; Zhou, J.; Hao, H.; Li, W. Controlled Synthesis of $Fe_2O_3$ modified $Ag$-$_{010}BiVO_4$ Heterostructures with Enhanced Photoelectrochemical Activity toward the Dye Degradation. *Appl. Surf. Sci.* **2017**, *399*, 1−9.
(13) Huang, C.-K.; Wu, T.; Huang, C.-W.; Lai, C.-Y.; Wu, M.-Y.; Lin, Y.-W. Enhanced Photocatalytic Performance of $BiVO_4$ in Aqueous $AgNO_3$ Solution under Visible Light Irradiation. *Appl. Surf. Sci.* **2017**, *399*, 10−19.
(14) Wu, C.; Fang, Y.; Tirusew, A. H.; Xiang, M.; Huang, Y.; Chen, C. Photochemical Oxidation Mechanism of Microcystin-RR by P-N Heterojunction $Ag/Ag_2O$-$BiVO_4$. *Chin. J. Catal.* **2017**, *38*, 192−198.
(15) Zhong, D. K.; Cornuz, M.; Sivula, K.; Grätzel, M.; Gamelin, D. R. Photo-Assisted Electrodeposition of Cobalt−Phosphate (Co−Pi) Catalyst on Hematite Photoanodes for Solar Water Oxidation. *Energy Environ. Sci.* **2011**, *4*, 1759−1764.
(16) Seabold, J. A.; Choi, K.-S. Effect of a Cobalt-Based Oxygen Evolution Catalyst on the Stability and the Selectivity of Photo-Oxidation Reactions of a $WO_3$ Photoanode. *Chem. Mater.* **2011**, *23*, 1105−1112.
(17) Zhao, Z.; Li, Z.; Zou, Z. Electronic Structure and Optical Properties of Monoclinic Clinobisvanite $BiVO_4$. *Phys. Chem. Chem. Phys.* **2011**, *13*, 4746−4753.
(18) Valenti, M.; Kontoleta, E.; Digdaya, I. A.; Jonsson, M. P.; Biskos, G.; Schmidt-Ott, A.; Smith, W. A. The Role of Size and Dimerization of Decorating Plasmonic Silver Nanoparticles on the Photoelectrochemical Solar Water Splitting Performance of $BiVO_4$ Photoanodes. *ChemNanoMat* **2016**, *2*, 739−747.
(19) Fang, L.; Nan, F.; Yang, Y.; Cao, D. Enhanced Photoelectrochemical and Photocatalytic Activity in Visible-Light-Driven $Ag/BiVO_4$ Inverse Opals. *Appl. Phys. Lett.* **2016**, *108*, 093902.
(20) Wang, M.; Lu, W.; Chen, D.; Liu, J.; Hu, B.; Jin, L.; Lin, Y.; Yue, D.; Huang, J.; Wang, Z. Synthesis of Dendritic-Like $BiVO_4$: Ag Heterostructure for Enhanced and Fast Photocatalytic Degradation of RhB Solution. *Mater. Res. Bull.* **2016**, *84*, 414−421.
(21) Du, M.; Xiong, S.; Wu, T.; Zhao, D.; Zhang, Q.; Fan, Z.; Zeng, Y.; Ji, F.; He, Q.; Xu, X. Preparation of a Microspherical Silver-Reduced Graphene Oxide-Bismuth Vanadate Composite and Evaluation of Its Photocatalytic Activity. *Materials* **2016**, *9*, 160.
(22) Gan, J.; Rajeeva, B. B.; Wu, Z.; Penley, D.; Liang, C.; Tong, Y.; Zheng, Y. Plasmon-Enhanced Nanoporous $BiVO_4$ Photoanodes for Efficient Photoelectrochemical Water Oxidation. *Nanotechnology* **2016**, *27*, 235401.
(23) Zhang, L.; Herrmann, L. O.; Baumberg, J. J. Size Dependent Plasmonic Effect on $BiVO_4$ Photoanodes for Solar Water Splitting. *Sci. Rep.* **2015**, *5*, 16660.
(24) Trzciński, K.; Szkoda, M.; Sawczak, M.; Karczewski, J.; Lisowska-Oleksiak, A. Visible Light Activity of Pulsed Layer Deposited $BiVO_4/MnO_2$ Films Decorated with Gold Nanoparticles: The Evidence for Hydroxyl Radicals Formation. *Appl. Surf. Sci.* **2016**, *385*, 199−208.
(25) Hirakawa, H.; Shiota, S.; Shiraishi, Y.; Sakamoto, H.; Ichikawa, S.; Hirai, T. Au Nanoparticles Supported on $BiVO_4$: Effective Inorganic Photocatalysts for $H_2O_2$ Production from Water and $O_2$ under Visible Light. *ACS Catal.* **2016**, *6*, 4976−4982.
(26) Yan, R.; Chen, M.; Zhou, H.; Liu, T.; Tang, X.; Zhang, K.; Zhu, H.; Ye, J.; Zhang, D.; Fan, T. Bio-Inspired Plasmonic Nano-architectured Hybrid System Towards Enhanced Far Red-to-Near Infrared Solar Photocatalysis. *Sci. Rep.* **2016**, *6*, 20001.
(27) Toma, F. M.; Cooper, J. K.; Kunzelmann, V.; McDowell, M. T.; Yu, J.; Larson, D. M.; Borys, N. J.; Abelyan, C.; Beeman, J. W.; Yu, K. M.; Yang, J.; Chen, L.; Shaner, M. R.; Spurgeon, J.; Houle, F. A.; Persson, K. A.; Sharp, I. D. Mechanistic Insights into Chemical and Photochemical Transformations of Bismuth Vanadate Photoanodes. *Nat. Commun.* **2016**, *7*, 12012.
(28) Lee, M. G.; Kim, D. H.; Sohn, W.; Moon, C. W.; Park, H.; Lee, S.; Jang, H. W. Conformally Coated $BiVO_4$ Nanodots on Porosity-Controlled $WO_3$ Nanorods as Highly Efficient Type II Heterojunction Photoanodes for Water Oxidation. *Nano Energy* **2016**, *28*, 250−260.
(29) Wang, Q.; Hisatomi, T.; Jia, Q.; Tokudome, H.; Zhong, M.; Wang, C.; Pan, Z.; Takata, T.; Nakabayashi, M.; Shibata, N.; Li, Y.; Sharp, I. D.; Kudo, A.; Yamada, T.; Domen, K. Scalable Water Splitting on Particulate Photocatalyst Sheets with a Solar-to-Hydrogen Energy Conversion Efficiency Exceeding 1%. *Nat. Mater.* **2016**, *15*, 611−615.
(30) Pastoriza-Santos, I.; Liz-Marzán, L. M. Formation and Stabilization of Silver Nanoparticles through Reduction by N, N-Dimethylformamide. *Langmuir* **1999**, *15*, 948.
(31) Palik, E. D. *Handbook of Optical Constants of Solids*, 1st ed.; Academic Press: New York, 1985.
(32) Kleemann, W. Absorption of Colloidal Silver in KCl. *Z. Phys.* **1968**, *215*, 113−120.
(33) Russell, B. K.; Mantovani, J. G.; Anderson, V. E.; Warmack, R. J.; Ferrell, T. L. Experimental Test of the Mie Theory for Microlithographically Produced Silver Spheres. *Phys. Rev. B: Condens. Matter Mater. Phys.* **1987**, *35*, 2151.
(34) Mock, J. J.; Smith, D. R.; Schultz, S. Local Refractive Index Dependence of Plasmon Resonance Spectra from Individual Nanoparticles. *Nano Lett.* **2003**, *3*, 485−491.
(35) Kamiyoshi, K.; Nigara, Y. Dielectric Constant of Some Alkali Halides. *Phys. Status Solidi A* **1970**, *3*, 735−741.
(36) Valant, M.; Suvorov, D. Chemical Compatibility between Silver Electrodes and Low-Firing Binary-Oxide Compounds: Conceptual Study. *J. Am. Ceram. Soc.* **2000**, *83*, 2721−2729.
(37) Thimsen, E.; Le Formal, F.; Grätzel, M.; Warren, S. C. Influence of Plasmonic Au Nanoparticles on the Photoactivity of $Fe_2O_3$ Electrodes for Water Splitting. *Nano Lett.* **2011**, *11*, 35−43.
(38) Thomann, I.; Pinaud, B. A.; Chen, Z.; Clemens, B. M.; Jaramillo, T. F.; Brongersma, M. L. Plasmon Enhanced Solar-to-Fuel Energy Conversion. *Nano Lett.* **2011**, *11*, 3440−3446.


DOI: 10.1021/acs.jpcc.8b00220
*J. Phys. Chem. C* 2018, 122, 7088−7093